A technique for spatial resolution improvement in helium-beam radiography

C. Amato[a)]
Department of Medical Physics in Radiation Oncology, German Cancer Research Center (DKFZ), Heidelberg, Germany
Heidelberg Institute for Radiation Oncology (HIRO), National Center for Radiation Research in Oncology (NCRO), Heidelberg, Germany
Department of Physics, University of Pisa, Pisa, Italy

M. Martisikova
Department of Medical Physics in Radiation Oncology, German Cancer Research Center (DKFZ), Heidelberg, Germany
Heidelberg Institute for Radiation Oncology (HIRO), National Center for Radiation Research in Oncology (NCRO), Heidelberg, Germany

T. Gehrke
Department of Medical Physics in Radiation Oncology, German Cancer Research Center (DKFZ), Heidelberg, Germany
Heidelberg Institute for Radiation Oncology (HIRO), National Center for Radiation Research in Oncology (NCRO), Heidelberg, Germany
Department of Physics and Astronomy, Heidelberg University, Heidelberg, Germany

(Received 21 May 2019; revised 10 January 2020; accepted for publication 11 January 2020; published 10 March 2020)

Purpose: Ion-beam radiography exhibits a significantly lower spatial resolution (SR) compared to x-ray radiography. This is mostly due the multiple Coulomb scattering (MCS) that the ions undergo in the imaged object. In this work, a novel technique to improve the spatial resolution in helium-beam radiography was developed. Increasing helium-beam energies were exploited in order to decrease the MCS, and therefore increase the SR.
Methods: The experimental investigation was carried out with a dedicated ion-tracking imaging system fully composed of thin, pixelated silicon detectors (Timepix). Four helium beams with increasing energies (from 168.8 to 220.5 MeV/u) were used to image a homogeneous 160 mm PMMA phantom with a 2 mm air gap at middle depth. An energy degrader (ED) was placed between the rear tracking system and the energy-deposition detector to compensate for the longer range associated with more energetic ions. The SR was measured for each beam energy. To take into account the overall impact on the image quality, the contrast-to-noise ratio (CNR), the single-ion water equivalent thickness (WET) precision and the absorbed dose in the phantom were also evaluated as a function of the initial beam energy. FLUKA Monte Carlo simulations were used to support the conceptual design of the experimental setup and for dose estimation.
Results: In the investigated energy interval, a total SR increase by around 30% was measured with increasing beam energy, reaching a maximum value of 0.69 lp/mm. For radiographs generated with 350 μGy of absorbed dose and 220 μm pixel size, a CNR decrease of 32% was found as the beam energy increases. For 1 mm pixel size, the CNR decreases only by 22%. The CNR of the images was always above 6. The single-ion WET precision was found to be in a range between 1.2% and 1.5%.
Conclusions: We have experimentally shown and quantified the possibility of improving SR in helium-beam radiography by using increasing beam energies in combination with an ED. A significant SR increase was measured with an acceptable decrease of CNR. Furthermore, we have shown that an ED can be a valuable tool to exploit increasing beam energies to generate energy-deposition radiographs. © *2020 The Authors. Medical Physics published by Wiley Periodicals, Inc. on behalf of American Association of Physicists in Medicine.* [https://doi.org/10.1002/mp.14051]

Key words: energy degrader, helium-beam radiography, ion-beam imaging, ion-beam radiotherapy, silicon pixel detector, spatial resolution

1. INTRODUCTION

The possibility to exploit ion beams for imaging purposes was already proposed in 1964[1] and soon afterwards the first experiment was performed with a proton beam and a radiographic film.[2] Fifty years after the first ion-beam radiography (iRad), iRads continue to show high contrast but nonetheless lower spatial resolution (SR) with respect to x-ray radiographs,[3–5] even despite the technological evolution and improvement of detectors. The limited SR achievable is still the main challenge today that research has to address.[6] This issue is the result of multiple Coulomb scattering (MCS) that ions undergo while traveling through the imaged object[7]: due to interactions between the ions and the field of target nuclei, the particle paths deviate from a straight line. This introduces uncertainties in the reconstruction of the radiographs and degrades the SR. The challenge of increasing the SR has been

addressed many times during the past three decades and the experimental setups over the years have been improved starting from a simple radiographic films to setups with dedicated detectors.

In the field of proton radiography (pRad) and computed tomography (pCT), the common approach adopted by many groups[8,9] nowadays is the single-proton tracking: position-sensitive detectors are used to measure the directions and positions of protons impinging and exiting the phantom, whereas the residual energy, or range, of each ion is detected by a range telescope, a calorimeter or a combination of the two.[9] For each proton, the particle positions and directions are detected upstream and downstream of the phantom. This information is used to reconstruct the most likely path (MLP) of the proton inside the imaged phantom.[10–12] The usage of MLP algorithms was demonstrated to provide higher SR than when using straight lines or cubic splines for modeling the particle paths.[13] Then, pRad or pCT images are generated by processing the reconstructed paths and detected energy information.

When heavier carbon ions are used as imaging radiation, the MCS inside the phantom is often neglected, and the experimental apparatus consists only of a position-sensitive detector for residual-energy measurements placed behind the imaged object.[14,15] For carbon-ion imaging, the main limitations are the high dose per ion in the phantom, and the fragmentation of primary ions, that leads to a decrease of the number of transmitted ions. These factors limit the image quality attainable within an acceptable patient dose.[16,17]

A helium-ion beam represents a compromise between p and ^{12}C imaging radiations. Helium ions undergo less MCS than protons because they are four times heavier, and in addition, they exhibit less fragmentation and deposit less dose per ion than carbon ions. In Gehrke et al.,[17] radiographs with protons, helium, and carbon ions were compared directly concerning SR, contrast-to-noise ratio (CNR) and absorbed dose. The CNR is the ratio between the contrast and the noise of the image, defined as:

$$CNR = \frac{|\langle S_1\rangle - \langle S_2\rangle|}{\sqrt{\sigma_{S_1}^2 + \sigma_{S_2}^2}}, \tag{1}$$

where $\langle S_i\rangle$ and σ_{S_i} are the mean and the standard deviation of pixel values in two homogeneous regions of interest (ROIs) of the image, respectively. Despite the higher SR provided by carbon ions, helium ions were shown to be the most suitable candidate for imaging purposes when also taking into account the CNR of the radiographs at the same clinically applicable absorbed dose.[17]

As already mentioned, the usage of single-ion tracking systems and MLP algorithms can improve the estimation of particle position inside the phantom, resulting in a higher SR. The approach to improve the SR investigated in this work is to increase the initial energy of the imaging beam which would allow decreasing the MCS experienced by the ions in the imaged object. For an incoming ion beam in z direction with no initial lateral and angular spread, the distribution of lateral displacement (in the perpendicular y direction) after having crossed a target with radiation length X_0 placed between z_0 and z_1 is approximately Gaussian with the variance[11]:

$$\sigma_y^2(z_0, z_1) = \frac{Z_p^2 E_0^2}{c^2 X_0}\left(1 + 0.038 \ln\frac{z_1 - z_0}{X_0}\right)^2 \int_{z_0}^{z_1} \frac{(z_1 - z)^2}{\beta^2(z) p^2(z)} dz, \tag{2}$$

where Z_p is the charge number of the incoming ion and $p(z)$ and $\beta(z)$ are the momentum and velocity of the ion at depth z inside the target. E_0 is an empirical constant equal to 13.6 MeV. Because of the $(\beta^2(z)p^2(z))^{-1}$ dependence in the integral, increasing the initial energy of the ions has the effect of decreasing the lateral displacement of ions in the phantom. Therefore, an increase in SR is expected with increasing beam energies.[3] This effect was experimentally and systematically investigated in this study for the first time. A single-ion tracking prototype system for iRad[18] was used to image a head-sized PMMA phantom with increasing beam energy. A sole increase in beam energy would lead to a severe loss of image contrast and WET resolution. This happens because a deeper position of the Bragg peak is associated with higher initial energies and the deployed apparatus exploits the steep rising part of the Bragg peak at a thin energy detector as source of contrast (see Section 2.A). Therefore, a technique was developed to overcome this obstacle. An energy degrader (ED) (copper slab) was integrated into the apparatus in front of the energy-deposition detector. The thickness of the ED increases as the beam energy increases ensuring that the steep rising part of the Bragg peak stays at the energy-deposition detector. To assess the effectiveness of this technique for the investigated energy interval, the fundamental image properties SR, CNR, and absorbed dose were evaluated. The precision of the system in measuring water equivalent thickness (WET) was also evaluated. Monte Carlo simulations were performed to support the optimization of the beam energy and of the ED thickness and for dose estimation.

2. MATERIALS AND METHODS

2.A. Imaging apparatus and acquisition technique

In this work, a single-ion imaging system recently developed within the Heidelberg Institute for Radiation Oncology[17,18] was used. For each ion that crosses the whole detection system, the position, the direction and the time of arrival are measured before impinging and after exiting the imaged object. Then, the energy deposition in an additional thin detector is measured. The different WETs of the imaged object are measured as different energy depositions. In order to optimize the sensitivity to small WET changes, the steep rising part of the Bragg curve has to be positioned at the detector for energy-deposition measurements. If this *operating principle* is satisfied, the steep rising part of the Bragg curve can be exploited as source of contrast and small WET differences are translated into relatively high differences in energy depositions measured by the detector (Fig. 1).

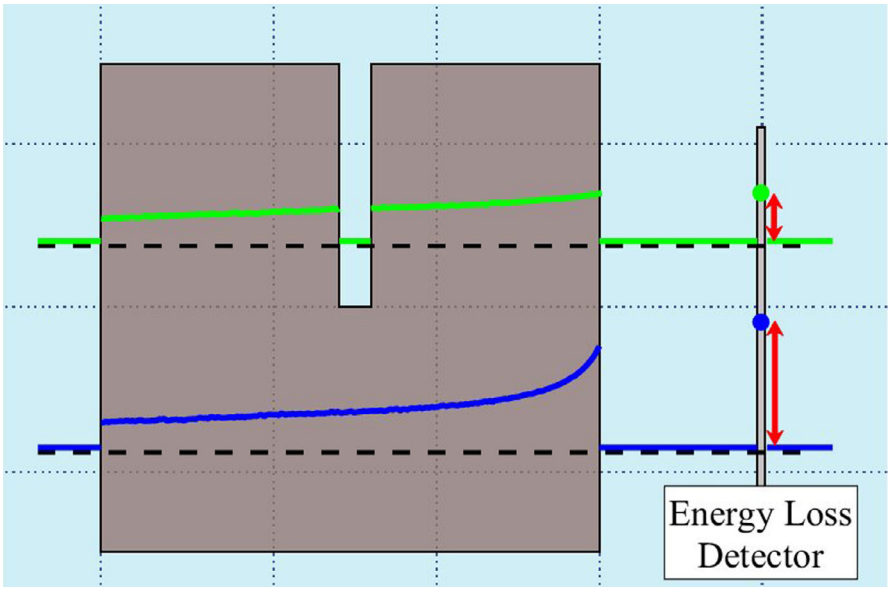

FIG. 1. Schematic illustration (not to scale) of the operating principle of the apparatus. The green line is the Bragg curve (with respect to the dashed lines) corresponding to ions that had crossed the air gap. The blue line is the Bragg curve of ions that had not crossed the air gap, and had lost more energy in the phantom. The two different energy depositions measured by the detector are highlighted with arrows. [Color figure can be viewed at wileyonlinelibrary.com]

In this investigation, the initial energy of the helium beam was increased in three steps, from 168.8 MeV/u up to 220.5 MeV/u to decrease MCS, which potentially leads to an improvement of SR. For the given phantom, 168.8 MeV/u is the beam energy that satisfies the operating principle (see findings in Section 3.A), whereas 220.5 MeV/u is currently the maximum energy for helium ions available at the accelerator of the Heidelberg Ion-Beam Therapy Center. Other expected effects related to increasing beam energies are a decrease in the absorbed dose in the imaged object and an increase in the energy-loss straggling and of the range straggling. These effects were quantified in Section 3.C. The increase of the beam energy leads also to a deeper position of the Bragg peak along the beam axis. To compensate for this effect, an ED was placed in front of the energy-deposition detector. The optimization of the ED thickness with respect to the beam energy was carried out through MC simulations (Section 3.A). The ideal properties of the ED should include a high relative stopping-power (RSP), a good and precise machinability, and a reasonable price. The high RSP is required to keep the thickness of the ED as thin as possible to maximize the geometrical acceptance, since MCS also takes place in the ED. Five candidate materials were investigated in order to choose the best one for the experimental application: water, PMMA, lead, tungsten, and copper. Water and PMMA were discarded because of their low RSP. Lead exhibits difficulties in the achievable precision of the machinability. Tungsten is relatively expensive and improvements with respect to copper (Cu) are only minor. Therefore, EDs made of Cu (purity higher than 99%) were used in the experiments.

The apparatus is one of the first iRad systems worldwide fully composed of pixelated silicon detectors (another example can be found in Pettersen et al.[19]). All the deployed detectors are Timepix, which were purchased from ADVACAM s.r.o., Prague, Czech Republic. The Timepix is a semiconductor detector developed at CERN by the Medpix2 Collaboration.[20] The deployed detectors consist of a sensitive silicon layer with an area of 1.4 cm × 1.4 cm and a thickness of 300 μm that is bump-bonded to a thinned read-out chip, which is 100 μm thick. The detector is divided into 256 × 256 pixels, with a pitch of 55 μm. A bias voltage of 10 V and a frame duration of 1 ms were used during the experiments as suggested in Gehrke et al.[21] Each detector can measure the time of arrival (time-mode) or the deposited energy (energy-mode) of the impinging particle.

As depicted in Fig. 2, the six Timepix detectors are arranged in 3 modules:

1. Two modules, called trackers in the following, that measure the position, the direction and the time of arrival of each particle impinging and exiting the phantom. The front tracker consists of detectors #1 and #2, whereas the rear tracker consists of detectors #3 and #4. These detectors work in time-mode.
2. One module for energy-deposition measurement: detector #5 works in energy mode and measures the energy deposited in the sensitive layer by each ion. To do so, a pixelwise calibration of the detector response was used.[22] Due to the lack of time information in energy-mode, the detector #5 had to be coupled with an additional detector (#6), that works in time-mode and measures the ions' time of arrival on this module.

Within each module, the two respective detectors are approximately 3.5 mm apart. The distances from the phantom surfaces were 2.9 and 4.4 cm for the detector #2 and #3, respectively. Each module is connected to its own read-out

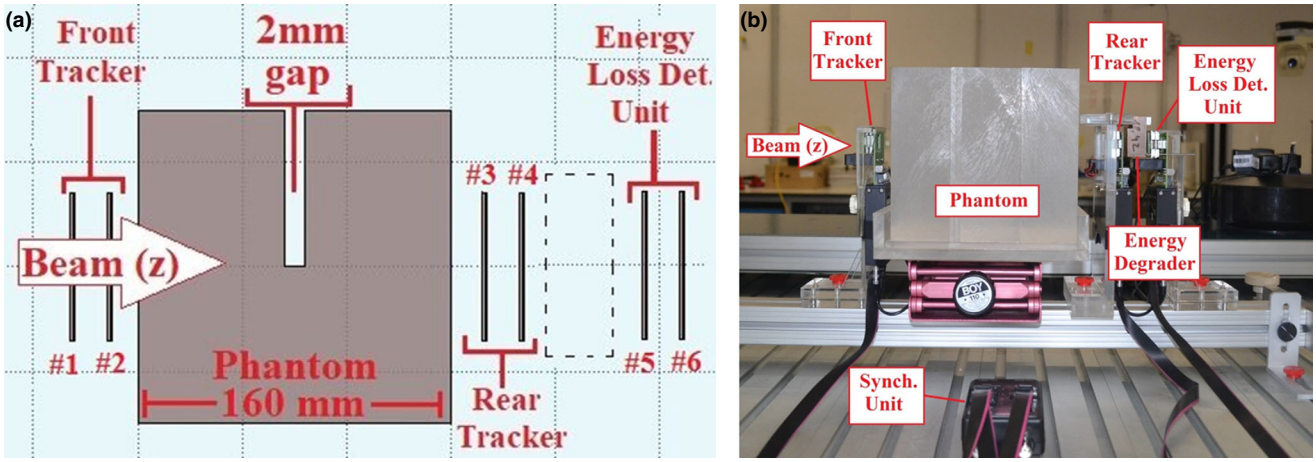

FIG. 2. (a) Schematic illustration (not to scale) of the radiography apparatus with the 2 mm gap to be imaged. The dashed box indicates the location of the ED, when deployed. (b) Picture of the experimental apparatus in the experimental room of the Heidelberg Ion Beam Therapy Center facility. [Color figure can be viewed at wileyonlinelibrary.com]

interface.[23] The three read-out interfaces are connected to a synchronization unit [Fig. 2(b)] in order to allow the tracking of ions all along the apparatus. Each read-out interface is then connected via USB2.0 to the PC, which is used to control the detectors by the software package Pixet.[24]

In previous publications,[17,18] the performance of the system was evaluated using a PMMA edge phantom (160 mm thick with an air gap of 1 mm placed in the middle) with a 168.8 MeV/u helium beam, reaching a density resolution of 0.6% and an average SR of 0.5 lp/mm. In these publications, only five Timepix detectors were used and the detector working in energy mode was integrated in the rear tracker module. In this work, the energy deposition detector had to be arranged in a new module with the detector #6 in order to make room for the ED [dashed box in Fig. 2(a)]. The ED was placed between the rear tracker and energy-deposition modules, so that the ions exiting the phantom are tracked at high velocity, before they were slowed down and scattered by the ED. Another change made with respect to previous publications is that the thickness of the air gap in the phantom was increased to 2 mm in order to decrease the relative image noise and thus have a more precise estimation of the SR. Otherwise, the phantom remained unchanged in order to enable reproducible and standardized measurements of SR and CNR, which can be difficult in anthropomorphic phantoms.

The measurements were performed at the Heidelberg Ion Beam Therapy Center (HIT).[25] The imaging apparatus was positioned in front of a fixed horizontal beamline, with detector #5 at the isocenter. Helium beams with four different energies were used (168.8, 185.3, 202.4 and 220.5MeV/u). In order to avoid signal pile-up, the mean fluence rate of the beam was reduced to be in the order of 4×10^4He-ions/s/cm^2. A beam focus of 10 mm (FWHM) was used.

2.B. Monte Carlo Simulations

Monte-Carlo (MC) simulations were used both to optimize experimental parameters and to estimate the absorbed dose in the imaged object. The apparatus and the beam were implemented using the FLUKA code.[26,27] The structure of each detector was simulated in accordance to Gehrke et al.[21] The sensitive layer and the read-out chip were simulated as silicon slabs with thicknesses of 300 and 100 μm, respectively. The two slabs were connected through a 256 × 256 matrix of spheres of 25 μm diameter, made of a tin–lead alloy. The helium beam was modeled with lateral dimensions of 1.4 cm × 1.4 cm. The beam origin was positioned 140 cm upstream of detector #3 in negative z direction [see Fig. 2(a)], according to the experimental setup. The ions were generated with a direction parallel to the *z*-axis and a momentum spread of 0.1%.[28]

The simulations of the whole experimental setup were used to optimize the beam energy and the ED thickness in order to satisfy the operating principle of the system. For beam energies of around 170 MeV/u, no ED is required, and the relative position between the Bragg peak and detector #5 was adjusted by changing just the beam energy. In this case, the beam energy was varied in the range 167.1–170.6 MeV/u in seven steps according to the discrete energy values available at the HIT accelerator. In the scenarios where the beam energy is higher and an ED is required, the relative position between the Bragg peak and detector #5 was adjusted by changing the ED thickness at a fixed beam energy. For the three energies used (185.3, 202.4 or 220.5 MeV/u), an initial guess of the copper-ED thickness was made using the SRIM software[29] and then it was varied in a range of ±8 mm. For each simulation, the number of simulated primary helium ions was fixed to 10^6, the radiograph of the edge phantom was reconstructed and the CNR was taken as figure of merit to evaluate if the operating principle was satisfied.

Additional simulations were performed to estimate the mean energy deposition per ion and the fluence as function of the penetration depth in silicon. The same helium beams described before to simulate the radiographs were used. The obtained curves were used in Section 3.A to visualize the

operating principle and to explain the relationship between the beam energy and the CNR of the final radiograph.

2.C. Data processing

The chain of data processing used to reconstruct iRads was introduced in earlier papers[17,18] and will be briefly described in the following.

First, based on the raw data from each detector, signals due to helium ions are identified and kept, whereas signals due to fragments and detector artifacts are rejected.[18] The importance of fragment identification in helium beam imaging and further approaches for different detector designs can be found in other literature.[30] For further analysis, in particular the dose estimation, it is necessary to define a quantity that relates the number of incoming helium ions (N_{Det1} = helium signals on detector #1) to the number of primary ions that crossed the full apparatus (N_{Det6} = helium signals on detector #6). This quantity was called transmission efficiency:

$$\eta^T = \frac{N_{Det6}}{N_{Det1}}. \tag{3}$$

Then, signals from different detectors due to the same helium ion have to be properly matched, in order to track ions along all the detection system. The matching of signals is initially performed between the detectors#1, #2, #3, #4 and #6 using a coincidence window of 400 ns. Subsequently, the matching process is extended to detector #5. The matching between signals recorded by detector #5 and detector #6 is based on the spatial information: a spatial window of 1.1 mm was used to compare impinging position of a helium ion on the two detectors. If signals caused by the same crossing helium ion are matched through all the six detectors, the event is called matched event. The matching efficiency of the whole process is defined as:

$$\eta^M = \frac{N_{match}}{N_{Det6}}, \tag{4}$$

where N_{match} is the total number of matched events. The matching efficiency η^M depends mostly on the incoming fluence rate of the helium ions: higher fluence rates lead to a higher number of pile-ups. These signals will be rejected during the signal identification and therefore the number of candidates for the matching will be reduced.

For each tracked ion, the path inside the phantom is reconstructed using the positions and directions measured by the front and the rear trackers. In this work, an approximation of the most likely path (MLP) for ions inside homogeneous targets by Fekete et al.[31] was used. The path is reconstructed with a third degree polynomial with optimized coefficients depending on the mean range of particles impinging onto the target and the total WET of the target.

The images are generated using a back-propagation algorithm called "along path reconstruction" (APR).[17] Examples of similar algorithms that exploit the ion path and residual range for image reconstruction can be found in Schneider et al.[32] and in Fekete et al.[33] For each measurement, the radiographs were reconstructed using a pixel size of 220 μm. In ion-beam treatment planning, x-ray CTs with 1mm pixel resolution and with 3 mm slice resolution are used.[34] In order to give CNR values for this therapy-relevant pixel size, radiographs were also reconstructed with 1 mm pixel size.

2.D. Image analysis

The fundamental quantities for evaluating the image quality are CNR and SR. For clinical application, also the dose delivered to the patient to obtain radiographs needs to be taken into account. The CNR of an image depends on the noise and consequently on the number of ions used to reconstruct the radiograph, which in turn is proportional to the imaging dose. Therefore, a fair comparison of the CNR of images obtained with different beam energies (E_{Beam}) requires radiographs with the same amount of absorbed dose. The dose was fixed to 350 μGy, a typical dose for a diagnostical x-ray head radiograph.[18,35] The number of matched events (N_{match}) corresponding to this dose level was estimated as follows:

$$N_{match} = \frac{350\mu\text{Gy}}{D_{ion}} * \eta^T * \eta^M, \tag{5}$$

where η^M is the matching efficiency, η^T is the transmission efficiency and D_{ion} is the dose per primary helium ion. The η^M and η^T were estimated experimentally, whereas the D_{ion} in MC simulations. As explained in Section 2.C, the matching efficiency η^M depends on the fluence rate of the beam, which can slightly fluctuate. For the nonstandard settings deployed to achieve a low fluence rate beam, the standard deviation of the fluence rate was found to be up to 30%. In order to avoid a deterioration of the results by this source of uncertainty, the mean matching efficiency of the four measurements (60%) was used for all beam energies. The transmission efficiency η^T, which is particularly dependent on the beam energy, was evaluated for each measurement. For each beam energy, eight radiographs were reconstructed using the same number of helium ions $N_{match}(E_{Beam})$. In each radiograph, the CNR was measured using regions of interest in the two homogeneous parts of the image. In the end, the CNR and its uncertainty were evaluated as the mean of the eight CNR values and the standard uncertainty of the mean.

Furthermore, to make results comparable to other detection systems, the single-ion WET precision[36] was evaluated as:

$$\sigma_{WET,i}(\%) = \frac{\sigma_{E_{dep},i}(\text{MeV})}{\mu_{WET,i}(\text{mm})} * \frac{\Delta\mu_{WET}(\text{mm})}{\Delta\mu_{E_{dep}}(\text{MeV})} * 100, \tag{6}$$

where the index i = {1,2} refers to the homogeneous ROI of the radiograph with the lower, higher WET, respectively; $\sigma_{E_{dep},i}$ and $\sigma_{WET,i}$ are the standard deviations of the distributions of single-ion energy depositions and WETs in the i-th ROI, respectively; $\mu_{E_{dep},i}$ and $\mu_{WET,i}$ denote the corresponding means; $\Delta\mu_{WET}/\Delta\mu_{E_{dep}}$ is an approximated calibration factor,

calculated as the ratio between the differences of the mean WETs and energy depositions of the two homogeneous regions of the radiographs. The approximation of taking the mean slope of the interval as calibration factor (instead of the actual slope of the calibration function) leads to an underestimation and overestimation of the WET precision in ROI 1 and 2, respectively. However, these two values provide a range for the single-ion WET precision for each beam energy.

For the evaluation of the SR, the edge was slightly tilted and the oversampling technique[37,38] was used to extract the edge profile. For each beam energy, the whole set of acquired data (around 4.1×10^5 events) was used to reconstruct a single radiograph in order to obtain the least noisy profile. The edge profile was fitted and processed as described in Gehrke et al.[17] to obtain the modulation transfer function (MTF). The SR was evaluated as the value of the spatial frequency at which the MTF is at 10% of its maximum value. The error on the SR was evaluated by propagating the uncertainty of the fit parameters (confidence interval of 68%).

3. RESULTS

3.A. Optimization of the beam energy and the ED thickness

The experimental setup was simulated (see Section 2.B) to choose the beam energies and the corresponding ED thicknesses which satisfy the operating principle (Fig. 1). In Figs. 3(a)–3(d) the CNR of the simulated radiographs was plotted for the four scenarios investigated: without ED (with variable beam energy) and for E_{beam} equal to 185.3, 202.4, and 220.5 MeV/u (with variable ED thickness). For each scenario, a broad peak of the CNR is visible.

Figures 4(a)–4(c) show the Bragg and the fluence curves simulated in silicon for E_{beam} equal to 170.6, 166.6, and

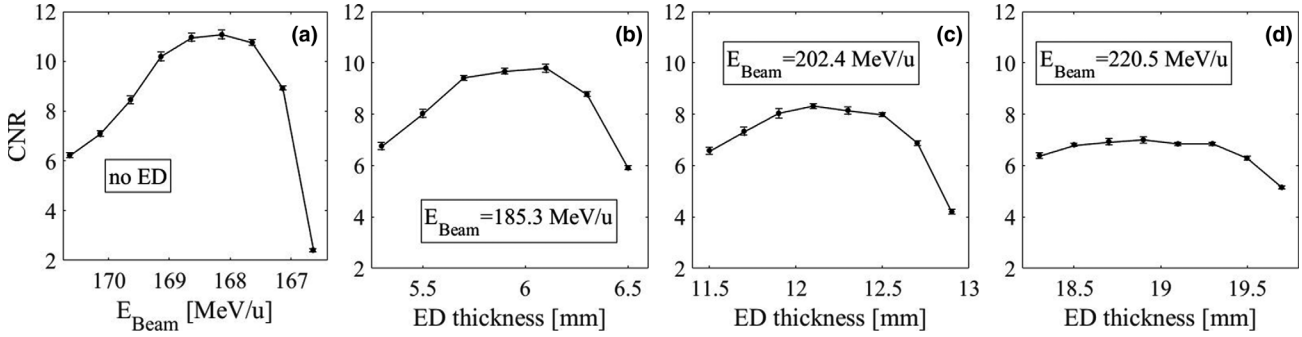

FIG. 3. (a) For the setup without energy degrader (ED), the contrast-to-noise ratio (CNR) of the edge phantom images is plotted as a function of E_{Beam} (reversed energy scale). (b–d) For E_{Beam} equal to 185.3 MeV/u (b), 202.4 MeV/u (c) and 220.5 MeV/u (d), the CNR is plotted as a function of the ED thickness.

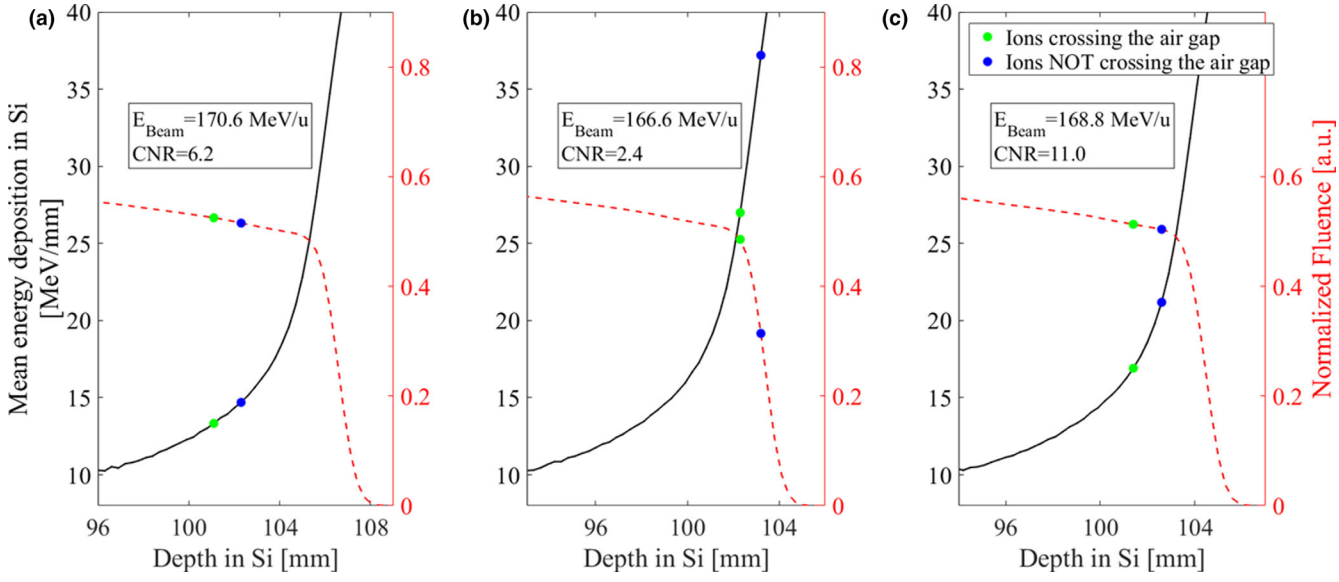

FIG. 4. Illustration of how the position of the Bragg peak with respect to the energy detector can influence the contrast-to-noise ratio of the final radiograph. The mean energy deposition per ion (black line) and the fluence curve (red dashed line) in silicon are shown for three different beam initial energies. In the corresponding radiographs, the mean energy depositions in the energy-deposition detector (det.#5) are shown as green points for helium ions that had crossed the air gap and as blue points for helium ions that had not. The corresponding points are highlighted on the fluence curve. [Color figure can be viewed at wileyonlinelibrary.com]

168.8 MeV/u. In the radiographs simulated with these beam energies, the mean energy depositions in detector 5 were evaluated for ions that did and did not cross the air gap. For each beam energy, these values were highlighted on the energy-deposition curve and the corresponding points were marked on the fluence curve. It can be seen that the beam energy of 170.6 MeV/u [Fig. 4(a)] is too high for the particular phantom. The two mean energy depositions are not in the steepest rising part of the Bragg curve, leading to relatively low contrast (CNR = 6.2). A beam energy of 166.6 MeV/u [Fig. 4(b)] is too low: despite that both mean energy depositions are located on the steep part of the Bragg curve, the corresponding fluence significantly drops. Therefore, the radiograph exhibits high noise, resulting in a low CNR (CNR = 2.4). The beam energy is properly adjusted at 168.8 MeV/u [Fig. 4(c)]: the energy-deposition measurement is performed in the steep part of the Bragg curve and right before the fluence drop. In this condition, the operating principle is satisfied and the optimal CNR is reached (CNR = 11.0). An effect that has to be underlined is that the CNR decrease due to the fluence drop is steeper than the one due to the too high beam energy. In Fig. 3,(a) a reverse x-axis was used in order to be consistent with Figs. 3(b)–3(d), and have the CNR decrease due to the fluence drop on the right side of the CNR peak.

According to the CNR peaks in Figs. 3(a)–3(d) and to the possibilities of ED machinability, the optimal combinations of beam energies and ED thicknesses were chosen (Table I). For the setup without ED [Fig. 3(a)], the two maximal points are comparable within the error. We have chosen the beam energy of 168.8 MeV/u in order to have a more robust optimization, that is, measuring under conditions that have a reduced probability of a drastic CNR decrease due to the fluence drop in case of discrepancies between simulations and experiments.

TABLE I. The investigated energies of the helium beam and the corresponding optimal thicknesses of the copper energy degrader.

E_{Beam} (MeV/u)	168.8	185.3	202.4	220.5
ED thickness (mm)	0	5.85	12.15	19.16

3.B. Spatial resolution

The experiments were performed using the four combinations of initial energy and ED thickness listed in Table I. The measured SR as a function of E_{Beam} is shown in Fig. 5 as a black line. A monotonic increase in the SR is observed. A total increase of $(29 \pm 5)\%$ [from (0.54 ± 0.01) lp/mm to (0.69 ± 0.02) lp/mm] was measured when the beam energy increased from 168.8 to 220.5 MeV/u. The results from measurements were also compared with FLUKA MC simulations. The simulated SR as a function of E_{beam} is shown in Fig. 5 as a red dotted line. A SR increase of $(34 \pm 4)\%$ [from (0.54 ± 0.01) lp/mm to (0.72 ± 0.01) lp/mm) is found when the energy is increased from 168.8 to 220.5 MeV/u. The simulated and the measured points are in agreement within their uncertainties.

3.C. Contrast-to-noise ratio and absorbed dose

The number of matched events required to reconstruct images with the same absorbed dose was estimated for each beam energy through Eq. (5). The values of the quantities involved are listed in Table II.

For radiographs with 220 μm pixel size and at the same absorbed dose of 350 μGy, the CNR as a function of the beam energy is shown in Fig. 6(a) as a black line. A total CNR decrease of $(32 \pm 2)\%$ is visible when the beam energy increases from 168.8 to 220.5 MeV/u. The radiograph with the lowest measured CNR is shown in Fig. 6(b) and is obtained with a beam energy of 220.5 MeV/u, an absorbed dose of 350 μGy and a pixel size of 220 μm.

The CNR decrease is due to the decrease in the difference between the two mean energy depositions $|\langle S_1 \rangle - \langle S_2 \rangle|$ and

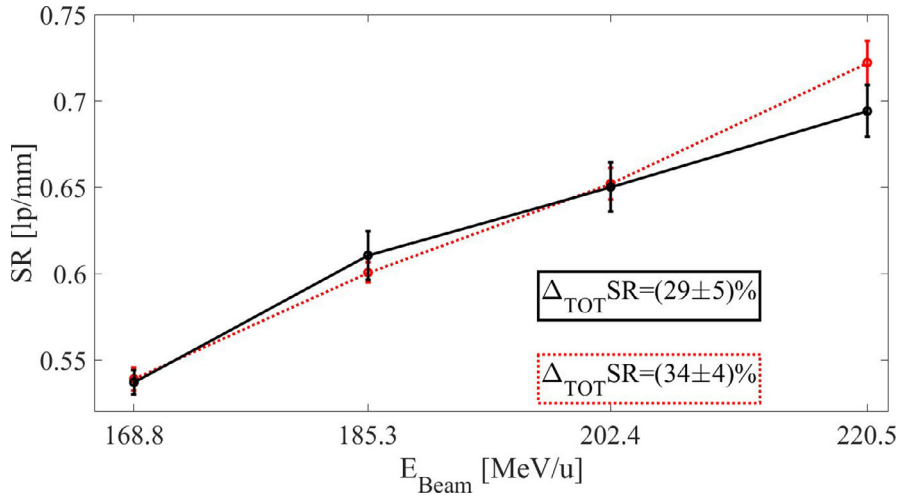

FIG. 5. Spatial resolution as a function of the beam energy for measurements (black line) and simulations (red dotted line). Relative spatial resolution increases are reported in the black and red box, respectively. [Color figure can be viewed at wileyonlinelibrary.com]

to the increase in the energy-deposition straggling $\sqrt{\sigma_{S_1}^2 + \sigma_{S_2}^2}$. With increasing beam energy in the investigated interval, the energy deposition difference decreases by (23 ± 2)%, whereas the straggling increases by (14 ± 4)%. These two effects contribute by approximately 60% and 40% to the observed CNR decrease, respectively. In the clinically relevant scenario where images are reconstructed with a pixel size of 1 mm, the CNR was evaluated and depicted as a function of the beam energy with a red dotted line in Fig. 6(a). In this case, the CNR is always higher than for images with 220 μm pixel size. This is due to the increased number of ions in each of the bigger pixels, which consequently leads to a decreased noise of the image. Because of this, for larger pixels the increase of the straggling plays a marginal role, and the total CNR decrease of (22 ± 6)% is almost completely (contribution close to 100%) due to the decrease of the difference between the two mean energy depositions.

3.D. Single-ion WET precision

The single-ion WET precision (Section 2.D) for both ROIs $\sigma_{WET,1}$ and $\sigma_{WET,2}$ and their mean $\overline{\sigma_{WET}}$ are summarized in Table III. The mean single-ion WET precision increases from 1.16% to 1.48% in the investigated energy interval.

TABLE II. Matching efficiency, transmission efficiency and dose per primary ion as a function of the helium-beam energy. The number of matched events required for radiographs with the same amount of absorbed dose (350 μGy) is calculated using Eq. (5).

E_{Beam} (MeV/u)	168.8	185.3	202.4	220.5
η^M (%)	60	60	60	60
η^T (%)	33.5	35.6	34.7	33.3
D_{ion} (nGy)]	1.986	1.686	1.511	1.379
N_{match} (10^3)	35.4	44.3	48.2	50.8

4. DISCUSSION

In this work, a novel technique was developed in order to increase the spatial resolution of helium-beam radiography. The beam energy was increased to decrease the amount of MCS within the imaged object and an ED was placed between the rear tracking system and the energy-deposition detector to compensate for the increasing range of ions. The Monte Carlo simulations were performed to optimize the beam energy and the ED thickness. The results have shown that the CNR of the radiograph can be used to determine whether or not the operating principle of the experimental apparatus is satisfied. Having the steep rising part of the Bragg peak at the energy-deposition detector ensures high sensitivity to small WET changes but also a limited range of measurable WETs. As shown in Figs. 4(a)–4(c), this is due to the relative position of the Bragg peak and fluence drop with respect to the energy-deposition detector.

Another finding of this study is that the range of measurable WET depends on the beam energy. As shown in Figs. 3(a)–3(d), the CNR peak becomes broader when the beam energy increases. When using a beam energy of 168.8 MeV/u and no ED, the CNR is constant (within ±5% of the maximum value) in an interval of 1.3 MeV/u, that corresponds approximately to a WET of 2.6 mm. When using a beam energy of 220.5 MeV/u and an ED of 19.16 mm, the CNR is almost constant in an interval of 0.94 mm of copper, which approximately corresponds to a WET of 5.6 mm.

TABLE III. Single-ion water equivalent thickness (WET) precision for regions of interest 1, 2 and their mean as a function of the beam energy.

E_{Beam} (MeV/u)	168.8	185.3	202.4	220.5
$\sigma_{WET,1}$(%)	1.11	1.22	1.31	1.43
$\sigma_{WET,2}$(%)	1.20	1.30	1.40	1.52
$\overline{\sigma_{WET}}$(%)	1.16	1.26	1.36	1.48

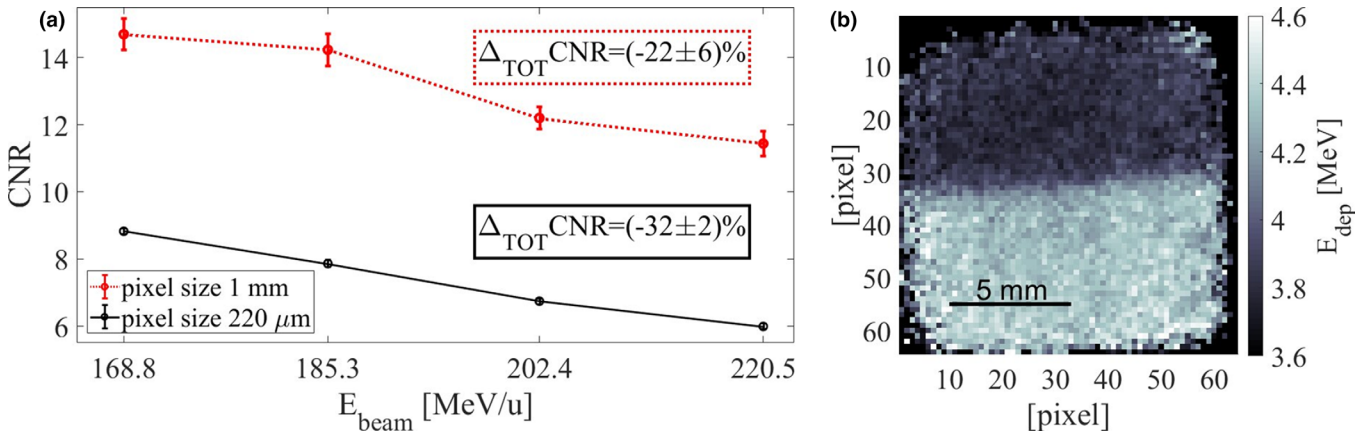

FIG. 6. (a) Contrast-to-noise ratio (CNR) as a function of the beam energy for radiographs with the same absorbed dose 350 μGy). The radiographs were reconstructed using 1 mm pixel size (red dotted line) and 220 μm pixel size (black line). The relative decreases of CNR are shown in boxes of the corresponding color. (b) The radiograph with the lowest CNR (CNR = 6). It was measured with a beam energy of 220.5 MeV/u, an absorbed dose of 350 and 220 μm pixel size. [Color figure can be viewed at wileyonlinelibrary.com]

An additional important benefit of using a higher beam energy is that the ED provides a safety margin, which prevents a change in the Bragg peak position into the patient in case of a significant WET change with respect to the planning CT. No significant activation of the ED above background levels was detected by the radiation safety commissioner after 8 h of experimentation.

A relevant increase in SR can be obtained through the increase in the beam energy and the usage of an ED. The ED was positioned between the rear tracker and the energy-deposition detector. The advantage of having faster ions is fully exploited by the trackers, before the ions are scattered and slowed down by the ED. To the authors' knowledge, this is the first time that an ED is used to improve the SR in such a way. Good agreement was found between the simulated and measured values. To the best of the authors' knowledge, the SR of 0.69 lp/mm measured in this work for a beam energy of 220.5 MeV/u is the highest SR for helium-beam imaging that can be found in the literature.[17,30,39]

For radiographs reconstructed with the same absorbed dose, the CNR showed a monotonic decreasing behavior with increasing beam energy. The decrease is more severe when small pixel sizes are used to reconstruct the radiographs. Despite the decrease, for a pixel size of 220 μm the CNR was measured to be always above 6 and, according to the Rose criterion,[40] the edge could be always resolved. For a pixel size of 1 mm, the CNR was always above 11, suggesting that in a clinical scenario the dose could be further reduced below 350 μGy maintaining an acceptable image quality.

The calculated single-ion WET precision is particular suited for making a comparison to other proton/ion-imaging detection systems with respect to WET resolution. The single-ion WET precision measured in this study ranges between 1.16% for the lowest beam energy and 1.48% for the highest. For similar WETs, other single-ion WET precision values that can be found in literature for proton detection systems are 1.6%,[36] 2.2%,[41] 2.7%,[42] 3.8%.[32] This translates to a single helium-ion precision of 0.8% to 1.9%. Since the novel technique using the highest beam energy and the thickest ED still provides a precision of 1.48% that is within this range, the observed shortfalls in WET precision for thicker EDs can be acceptable in order to increase the SR for certain situations in an envisaged clinical application. Furthermore, it was recently shown[41] that for heterogeneous objects with irregular surfaces MCS can be a dominant contribution to image noise. In this respect, the MCS decrease achieved thanks to the proposed technique could be beneficial not only for the SR, but also for the CNR. It can be speculated that this effect can partially compensate the CNR decrease observed in this study. This could not be observed in this study due to the simplified geometry of the deployed phantom. This limitation does not allow a conclusion on how the detection system would perform in cases of irregular surfaces and heterogeneities.

An additional limitation of the imaging system is the aforementioned range of measurable WETs. To overcome this limitation, a beam with variable optimized energy could be used to image a phantom with WET modulations that exceed the dynamic range of the apparatus. The area to be imaged can be divided into regions of around 2 cm^2 and, if in such a small region the WET modulation is <6 mm, an optimal beam energy can be chosen. A prior estimation of the region-by-region WET could be obtained by the x-ray CT that was previously acquired in the clinical workflow. In this way, a radiograph of objects with large WET modulation can be achieved. The technique deploying variable optimized energies would have also the advantage that only one ED plate is required, because the CNR optimization is reached via beam energy adjustment.

The developed technique helped to overcome one of the limitations of the previous apparatus.[17] In fact without an ED and for a given phantom thickness, there is only a narrow window of beam energies which satisfies the operating principle [as shown in Fig. 3(a)]. By deploying an ED, it is instead possible to exploit all the higher beam energies. The usage of an ED is of particular interest for setups using thin energy-deposition detectors. However, the relevance of the method is not restricted to such setups: it is also applicable to other single-ion tracking systems, for example, deploying a range telescope or a residual-energy detector, provided that there is a possibility to accommodate the ED between the rear tracker and the range telescope or residual-energy detector.

5. SUMMARY AND CONCLUSIONS

In this study, a technique for improving the SR of helium-beam radiography was developed.

An edge phantom 160 mm thick with a 2 mm air gap at middle depth was imaged using helium beams of increasing energy between 168.8 and 220.5 MeV/u. To compensate for the increasing range of ions, an energy degraded (ED) was implemented in an ion-imaging apparatus for the first time. Monte Carlo simulations were used to optimize the relationship between beam energy and ED thickness. It was shown that the contrast-to-noise ratio (CNR) of simulated radiographs can be used to precisely adjust the steep rising part of the Bragg curve at the energy-deposition detector, and therefore optimize the WET sensitivity during measurements. For image quality assessment, the radiographs were reconstructed from both measured and simulated data for the four increasing beam energies. The SR as a function of the increasing beam energy exhibits a monotonically rising behavior in the investigated energy range. A significant SR increase of 29% [from (0.54 ± 0.01) lp/mm to (0.69 ± 0.02) lp/mm] was measured for the whole beam-energy interval investigated, while from simulations, an SR increase of 34% was expected. An agreement between the simulated and the measured SR values was found within the uncertainty. The CNR was evaluated on radiographs generated with a clinically relevant absorbed dose (350 μGy). A total decrease of CNR by 32% was measured for radiographs with 220 μm pixel size. In the case of 1 mm pixel size, the CNR decreased by 22%. Despite the decrease, the CNR was found to be always above 6 and the imaged inhomogeneity could be always clearly resolved. A single-ion WET precision better than 1.48% was reached for all measurements. In conclusion, this work demonstrated experimentally that by deploying higher helium-beam

energies and an ED, an increase in SR can be achieved with an acceptable CNR decrease.

ACKNOWLEDGMENTS

The authors thank the HIT facility for the beam time and the special beam settings provided. We thank the whole team of Advacam s.r.o. for the support concerning the Timepix and FitPIX devices, Gernot Echner and the DKFZ workshop personnel for the manufacturing of the copper slabs and the detector-support system. TG was funded by the German Science Foundation (DFG, KFO 214, under the project number MA 4437/3-1).

CONFLICT OF INTEREST

The authors have no conflict to disclose.

[a)]Author to whom correspondence should be addressed. Electronic mail: carlo.amato@dkfz-heidelberg.de.

REFERENCES

1. Cormack AM. Representation of a function by its line integrals, with some radiological applications. II. *J Appl Phys*. 1964;35:2908–2913.
2. Koehler AM. Proton radiography. *Science (New York, N.Y.)*. 1968;160:303–304.
3. Johnson RP. Review of medical radiography and tomography with proton beams. *Rep Progr Phys*. 2018;81:016701.
4. Depauw N, Seco J. Sensitivity study of proton radiography and comparison with kV and MV x-ray imaging using GEANT4 Monte Carlo simulations. *Phys Med Biol*. 2011;56:2407–2421.
5. Schulte RW, Bashkirov V, Loss Klock MC, et al. Density resolution of proton computed tomography. *Med Phys*. 2005;32:1035–1046.
6. Poludniowski G, Allinson NM, Evans PM. Proton radiography and tomography with application to proton therapy. *Br J Radiol*. 2015;88:20150134.
7. Bethe HA. Molière's theory of multiple scattering. *Phys Rev*. 1953;89:1256–1266.
8. Pemler P, Besserer J, de Boer J, et al. A detector system for proton radiography on the gantry of the Paul-Scherrer-Institute. *Nucl Instrum Methods Phys Res Sect A*. 1999;432:483–495.
9. Bashkirov VA, Johnson RP, Sadrozinski HF-W, Schulte RW. Development of proton computed tomography detectors for applications in hadron therapy. *Nucl Instrum Methods Phys Res Sect A*. 2016;809:120–129.
10. Williams DC. The most likely path of an energetic charged particle through a uniform medium. *Phys Med Biol*. 2004;49:2899–2911.
11. Schulte RW, Penfold SN, Tafas JT, Schubert KE. A maximum likelihood proton path formalism for application in proton computed tomography. *Med Phys*. 2008;35:4849–4856.
12. Fekete C-AC, Doolan P, Dias MF, Beaulieu L, Seco J. Developing a phenomenological model of the proton trajectory within a heterogeneous medium required for proton imaging. *Phys Med Biol*. 2015;60:5071–5082.
13. Li T, Liang Z, Singanallur JV, Satogata TJ, Williams DC, Schulte RW. Reconstruction for proton computed tomography by tracing proton trajectories: a Monte Carlo study. *Med Phys*. 2006;33:699–706.
14. Telsemeyer J, Jäkel O, Martišíková M. Quantitative carbon ion beam radiography and tomography with a flat-panel detector. *Phys Med Biol*. 2012;57:7957–7971.
15. Rinaldi I, Brons S, Gordon J et al. Experimental characterization of a prototype detector system for carbon ion radiography and tomography. *Phys Med Biol*. 2013;58:413–427.
16. Parodi K. Heavy ion radiography and tomography. *Physica Medica*. 2014;30:539–543.
17. Gehrke T, Amato C, Berke S, Martišiková M. Theoretical and experimental comparison of proton and helium-beam radiography using silicon pixel detectors. *Phys Med Biol*. 2018;63:035037.
18. Gehrke T, Gallas R, Jäkel O, Martišíková M. Proof of principle of helium-beam radiography using silicon pixel detectors for energy deposition measurement, identification, and tracking of single ions. *Med Phys*. 2018;45:817–829.
19. Pettersen HES, Alme J, Biegun A, et al. Proton tracking in a high-granularity Digital Tracking Calorimeter for proton CT purposes; 2016.
20. Llopart X, Ballabriga R, Campbell M, Tlustos L, Wong W. Timepix, a 65k programmable pixel readout chip for arrival time, energy and/or photon counting measurements. *Nucl Instrum Methods Phys Res Sect A*. 2007;581:485–494.
21. Gehrke T, Burigo L, Arico G, et al. Energy deposition measurements of single 1 H, 4 He and 12 C ions of therapeutic energies in a silicon pixel detector. *J Instrum*. 2017;12:P04025.
22. Jakubek J. Precise energy calibration of pixel detector working in time-over-threshold mode. *Nucl Instrum Methods Phys Res Sect A*. 2011;633:S262–S266.
23. Kraus V, Holik M, Jakubek J, Kroupa M, Soukup P, Vykydal Z. FITPix — fast interface for Timepix pixel detectors. *J Instrum*. 2011;6:C01079.
24. Turecek D, Holy T, Jakubek J, Pospisil S, Vykydal Z. Pixelman: a multiplatform data acquisition and processing software package for Medipix2, Timepix and Medipix3 detectors. *J Instrum*. 2011;6:C01046.
25. Haberer TH, Debus J, Eickhoff H, Jäkel O, Schulz-Ertner D, Weber U. The Heidelberg Ion Therapy Center. *Radiother Oncol*. 2004;73:186–190.
26. Ferrari A, Sala PR, Fasso A, Ranft J. FLUKA: A multi-particle transport code (Program version 2005); 2005.
27. Battistoni G, Cerutti F, Fasso A, et al. The FLUKA code: description and benchmarking, in *AIP Conference Proceedings*, volume 896, pages 31–49, AIP; 2007.
28. Parodi K, Mairani A, Brons S, et al. Monte Carlo simulations to support start-up and treatment planning of scanned proton and carbon ion therapy at a synchrotron-based facility. *Phys Med Biol*. 2012;57:3759–3784.
29. Ziegler JF, Ziegler M, Biersack J. SRIM – the stopping and range of ions in matter (2010). *Nucl Instrum Methods Phys Res Sect B*. 2010;268:1818–1823.
30. Volz L, Piersimoni P, Bashkirov VA, et al. The impact of secondary fragments on the image quality of helium ion imaging. *Phys Med Biol*. 2018;63:195016.
31. Collins-Fekete C-A, Volz L, Portillo SKN, Beaulieu L, Seco J. A theoretical framework to predict the most likely ion path in particle imaging. *Phys Med Biol*. 2017;62:1777–1790.
32. Schneider U, Besserer J, Pemler P, et al. First proton radiography of an animal patient. *Med Phys*. 2004;31:1046–1051.
33. Collins-Fekete C-A, Brousmiche S, Portillo SKN, Beaulieu L, Seco J. A maximum likelihood method for high resolution proton radiography/proton CT. *Phys Med Biol*. 2016;61:8232–8248.
34. Schardt D, Elsässer T, Schulz-Ertner D. Heavy-ion tumor therapy: physical and radiobiological benefits. *Rev Modern Phys*. 2010;82:383–425.
35. Schegerer AA. Bekanntmachung der aktualisierten diagnostischen Referenzwerte fur diagnostische und interventionelle Rontgenanwendungen. Bundesamt fur Strahlenschutz, 2010; 2016.
36. Bashkirov VA, Schulte RW, Hurley RF, et al. Novel scintillation detector design and performance for proton radiography and computed tomography. *Med Phys*. 2016;43:664–674.
37. Fujita H, Tsai D-Y, Itoh T, et al. A simple method for determining the modulation transfer function in digital radiography. *IEEE Trans Med Imaging*. 1992;11:34–39.
38. Mori I, Machida Y. Deriving the modulation transfer function of CT from extremely noisy edge profiles. *Radiol Phys Technol*. 2009;2:22–32.
39. Volz L, Collins-Fekete C-A, Piersimoni P, et al. Stopping power accuracy and achievable spatial resolution of helium ion imaging using a prototype particle CT detector system. *Curr Direct Biomed Eng*. 2017;3:401–404.
40. Rose A. The sensitivity performance of the human eye on an absolute scale*. *J Opt Soc Am*. 1948;38:196.
41. Dickmann J, Wesp P, Rädler M, et al. Prediction of image noise contributions in proton computed tomography and comparison to measurements. *Phys Med Biol*. 2019;64:145016.
42. Pettersen HES, Alme J, Barnaföldi GG, et al. Design optimization of a pixel-based range telescope for proton computed tomography. *Physica Medica*. 2019;63:87–97.